Accessibility of the pores in highly porous alumina films synthesized via sequential infiltration synthesis

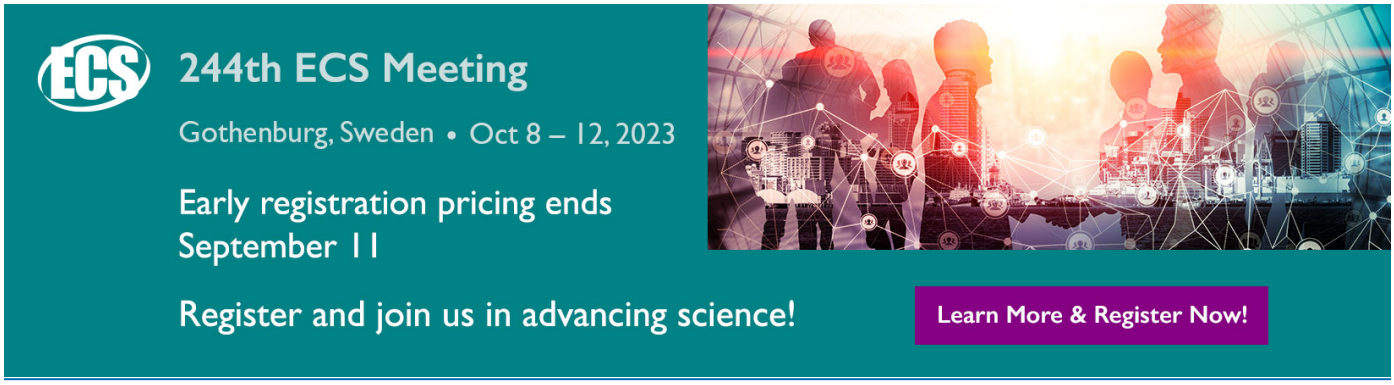

IOP Publishing Nanotechnology
Nanotechnology 29 (2018) 495703 (10pp) https://doi.org/10.1088/1361-6528/aae144

Accessibility of the pores in highly porous alumina films synthesized via sequential infiltration synthesis

Yunlong She[1], Jihyung Lee[1], Benjamin T Diroll[2], Thomas W Scharf[1], Elena V Shevchenko[2,3] and Diana Berman[1,3]

[1] Materials Science and Engineering Department and Advanced Materials and Manufacturing Processes Institute, University of North Texas, 1155 Union Circle, Denton, TX 76203, United States of America
[2] Center for Nanoscale Materials, Argonne National Laboratory, 9700 S. Cass Ave, Argonne, IL 60439, United States of America

E-mail: shevchenko@anl.gov and Diana.Berman@unt.edu

Received 20 August 2018
Accepted for publication 13 September 2018
Published 5 October 2018

Abstract

Inorganic nanoporous materials with highly accessible pores are of great interest for the design of efficient catalytic, purification and detection systems. Limited access to the pores is a common problem associated with traditional approaches for the synthesis of porous materials, affecting the functionality of the low-density structure. Recently, infiltration of a nanoporous polymer template with inorganic precursors followed by oxidative annealing was proposed as a new and efficient approach to creating porous inorganic structures with controlled thickness, composition and pore sizes. Here, we report an ultra-high accessibility of the pores in porous films prepared via polymer-swelling-assisted sequential infiltration synthesis (SIS). Using a quartz crystal microbalance technique, we show the increased solvent adsorbing capabilities of highly porous alumina films as a result of high interconnectivity of the pores in such structures. The directionality and highly interconnected nature of the pores are demonstrated in experiments with the partial blocking of pore access by the deposition of a single-layer graphene that is not transparent to solvent. 60% of the pores remain accessible when only 20% of the surface is exposed to solvent. Using humidity detection as an example, we also show that highly porous alumina produced by polymer-swelling-assisted SIS is a promising candidate for sensing applications.

Supplementary material for this article is available online

Keywords: porous alumina, water adsorption, humidity sensing, pores interconnectivity, graphene

(Some figures may appear in colour only in the online journal)

1. Introduction

Highly porous inorganic materials are of great interest for a broad range of applications, from optical coatings [1, 2] to catalysts [3–5], sensors [6, 7], and purification/separation systems [8]. Many of these applications benefit greatly from the accessibility of all pores for liquid or gas penetration [9]. The most common porous materials are zeolites [5, 8], oxides prepared by anodization of the corresponding metal [3, 10, 11] and ceramics prepared by a gel-casting process [12, 13]. Each class of porous materials has its own advantages and concerns. For example, the use of highly porous natural and artificial zeolites has a tremendous impact on technologically important processes such as catalytic reactions, ion exchange, and filtration. However, most of the zeolites have confined pores of a few atoms (~sub-nanometer in diameter) [5, 8]; this is associated with

[3] Authors to whom any correspondence should be addressed.

intracrystalline molecular transport limitations, resulting in low utilization of the zeolite active volume [4, 14, 15]. Pore structures prepared by anodization of corresponding metals [16–18] reveal pronounced directionality of the pores that can limit the access of media from their sides [3, 10, 11]. In turn, ceramics prepared by a gel-casting approach have randomly distributed nanosized pores formed as a result of the sintering of the individual small nanoparticles during synthesis [12, 13]. However, some pores cannot be accessed. Even though the introduction of sacrificial inclusions (e.g. carbon, etc) resulting in additional porosity at the expense formation of larger pores ($\geqslant$300 nm) improves the accessibility of nanopores [12], a fraction of them still remain unavailable.

Previously, sequential infiltration of the block-copolymer template with inorganic precursors using sequential infiltration synthesis (SIS) was proposed as a new technique for patterning ceramics with a nanosize resolution [19–23]. Originally, SIS allowed the synthesis of conformal coatings with thickness limitations dictated by the infiltration depth of the block polymer template (typically 40–50 nm). Recently, we demonstrated that the thickness can be substantially increased by introducing a swelling-of-the-polymer step [22, 23] that enables precise control of the dimensions and porosity of the resulting nanoporous alumina structures [23].

Here, we report on high accessibility and interconnectivity of the pores in nanoporous alumina films synthesized with polymer-swelling-assisted SIS [23]. Prompt estimation of the accessibility of the pores in porous structures without a need to synthesize large volumes of materials is critically important for rapid performance optimization and discovery of new materials in a cost- and time-efficient manner. We implement a quartz crystal microbalance (QCM) technique for analysis of the solvent penetration characteristics of ~200 nm thick nanoporous alumina films. Monitoring the change in the resonant frequency and mechanical resistance response of the QCM crystal with the deposited material upon exposure to different environments shows that highly porous (~70%) alumina films consist of highly interconnected pores. High accessibility of the pores in SIS-developed alumina, as confirmed by the experiment on blocking surface pore access using single-layer graphene, enables almost immediate water and acetone adsorption and leads to good performance of the material for humidity sensing.

2. Experimental procedure

2.1. Synthesis of nanoporous alumina films

Nanoporous alumina films were obtained via the SIS approach that is based on vapor phase infiltration of a swollen polystyrene-b-poly-2-vinyl pyridine (PS-p2VP) block-copolymer template, where the polar part of the polymer film acts as a selective site for the reactions to proceed [22, 23]. Briefly, titanium QCM electrodes were covered with PS-p2VP films with 1:2, 1:1, and 2:1 concentration ratios for polar and non-polar parts using spin-coating of the 3 wt% concentration of the polymers in toluene. After swelling of the polymers in ethanol (1 h at 75 °C), the films were exposed to subsequent cycling of trimethylaluminum (TMA) and water vapors resulting in selective infiltration of alumina inside the polar domains of the polymer, thus replicating a polymer structure. Specifically, the SIS was performed in the Cambridge Nanotech Inc. ALD system at 90 °C to avoid melting of swelling-formed predefined polymer structures. QCM substrates with polymer films were loaded on a stainless steel tray and kept at 100 sccm nitrogen flow for 30 min prior to deposition. One cycle of SIS was performed as follows: 10 mTorr of the TMA precursor was admitted with 20 sccm nitrogen flow into the reactor for 400 s; after the predetermined time when the infiltration of the polymer occurs the excess reactant was evacuated after which 10 mTorr of H_2O was admitted for 120 s; the chamber was then purged with 100 sccm of nitrogen to remove not-infiltrated byproducts. In total, 10 cycles of SIS were used to ensure full infiltration of the polymers with aluminum oxide. After infiltration, the polymer template was removed by a prolonged UV ozone cleaning technique (8 h), leaving nanoporous aluminum oxide films on the QCM surface. The samples were treated inside the UV ozone cleaner (UVOCST16x16 OES, 254 nm UV wavelength) for 24 h at room temperature. UV ozone was used instead of the previously reported thermal annealing-based removal of the polymer to prevent damage to the quartz crystals at high temperature. Complete removal of the polymer was confirmed with energy dispersive x-ray spectroscopy analysis (see supporting information, figure S1 is available online at stacks.iop.org/NANO/29/495703/mmedia).

2.2. Blocking porosity with graphene

Chemical vapor deposition (CVD) grown on copper foil single-layer graphene (Graphenea Inc.) was transferred onto the QCM surface coated with porous alumina using a wet chemistry transfer method [24]. The graphene was covered with a spin-coated 200 nm thick poly(methyl methacrylate) (PMMA) film. Then, the copper was etched in a copper etchant, and the resulting graphene with the PMMA film on top was transferred onto the QCM surface. The PMMA was removed with a warm acetone bath. During the transfer, encapsulation of the water in the pores and its evaporation during baking of the sample at 90 °C resulted in graphene rupture in multiple places. Complete removal of the PMMA layer and the single-layer nature of the graphene film were confirmed using scanning electron microscopy (SEM) and Raman spectroscopy with a 534 nm green laser. Overall, the procedure led to about 80% coverage of graphene film on top of the nanoporous alumina.

2.3. QCM analysis

The adsorption characteristics of the porous alumina were analyzed using the QCM technique by immersing the deposited QCM surface porous structure into the solvent (water and acetone). The QCM, made of an AT-cut piezoelectric quartz

crystal oscillating in a shear mode, reproduces in frequency and resistance change the response of the modification in the surface during sliding. AT-cut crystals (1 inch in diameter) oscillating in a shear mode with 5 MHz resonance frequency were chosen for the study. Titanium- and aluminum-coated QCMs were purchased from Fil-Tech. Changes in resonant frequency and mechanical resistance of QCM oscillations upon immersing in liquids, more viscous water, and less viscous acetone, were monitored using an SRS QCM 200 system.

In the classic approach for evaluating QCM frequency change under applied load, ideally a mooth surface of the QCM is assumed [25]:

$$\Delta f = -f_0^{3/2}\sqrt{\frac{\rho_L \eta_L}{\pi \mu_q \rho_q}} \quad (1)$$

where f_0 is the fundamental frequency of the QCM, $\rho_q = 2.648\ \mathrm{g\,cm^{-3}}$ is the density of quartz, $\mu_q = 2.947 \times 10^{11}\ \mathrm{g\ cm^{-1}\ s^{-2}}$ is the shear modulus of quartz and ρ_L, and η_L are the density and viscosity of the liquid, respectively. In the case of a QCM immersed in water, $\rho_L = 0.9982\ \mathrm{g\,cm^{-3}}$ and $\eta_L = 0.01\ \mathrm{g\ cm^{-1}\ s^{-1}}$. In the case of a QCM immersed in acetone, $\rho_L = 0.784\ \mathrm{g\,cm^{-3}}$ and $\eta_L = 0.003\ \mathrm{g\ cm^{-1}\ s^{-1}}$. Substituting density and viscosity values gives an estimate of the expected frequency shifts upon immersing in water and acetone to be 700 Hz and 360 Hz, respectively.

The mechanical resistance of the QCM measured in ohms is the resistance to be added to the oscillator circuit to sustain stable QCM oscillation [26]. For a QCM with an ideal smooth surface immersed in liquid, the mechanical resistance can be calculated as [27]:

$$\Delta R = (2fL_u)\sqrt{\frac{4\pi f \rho_L \eta_L}{\mu_q \rho_q}} \quad (2)$$

where L_u is inductance for the dry resonator. Expected mechanical resistance values are 320 and 160 Ω, respectively.

2.4. Characterization

Porosity and thickness values of the deposited alumina coatings were estimated from ellipsometry data (figure S2, SI), obtained with an M-2000V ellipsometer. Alumina thickness and porosity were estimated as ~200 nm and ~70%, 45%, and 30% for three different polymers respectively. The samples were further characterized using an FEI Nova Scanning Electron Microscope (SEM) with energy dispersion x-ray analysis to confirm complete removal of the polymer template and alumina composition of the porous structure (figure S1, SI). Transmission electron microscopy (TEM) was conducted using the JEOL2100F instrument. The alumina was scratched from the substrate and suspended in acetone. Next, a drop of this suspension was deposited onto the carbon coated copper mesh grid and dried. Contact angle measurements were conducted by the sessile water drop method using a ramé-hart 250 contact angle goniometer. Contact angle data were averaged based on five measurements for each sample. X-ray photoemission spectroscopy (XPS) analysis was performed with a PHI 5000 Versaprobe Scanning X-ray Spectrometer (figure S3, SI).

3. Results and discussion

Polymer-swelling-assisted SIS of the PS-p2VP block copolymer resulted in the formation of the conformal alumina coating. Figures 1(a)–(c) present SEM images of the resulting nanoporous alumina films with different porosity. The TEM image in figure 1(d) and the electron diffraction pattern in figure 1(d) inset reveal the amorphous nature of the porous alumina. Nanoporous alumina films were grown directly on the QCM titanium surface (figures 1(e) and (f)).

Water and acetone penetration of the nanoporous alumina films deposited on the QCM surface was tested by immersing the QCM surface into corresponding solvents. Our results demonstrate a more substantial drop in resonant frequency and increase in mechanical resistance than calculated based on equations (1) and (2) for all three samples, which assume (i) distinguishable interface between QCM and liquid and (ii) water adsorption inside the material (figure 2). Thus, in the case of porous materials, penetration of the solvent inside the structure affects the measurements, requiring the modification of equations (1) and (2). We do take into account that when trapped water is trapped for the lateral movement, the penetrating water will act as an additional mass for the QCM response [27]. In this case, equation (1) can be modified to:

$$\delta f = -f^{3/2}\sqrt{\frac{\rho_L \eta_L}{\pi \mu_q \rho_q}} - \frac{2f^2}{A\sqrt{\rho_q \mu_q}}\Delta m,$$

where Δm is the mass of water trapped inside the structure, and A is the effective surface area of the added mass. In our case, assuming that water fills 70%, 45%, and 30% of the 200 nm thick alumina film, the expected additional changes in frequency due to the added mass of water are ~800 Hz, ~510 Hz, and ~340 Hz; in the case of an added mass of acetone the frequency shifts are ~620 Hz, ~400 Hz, and ~260 Hz. Thus, QCM allows us to assess the efficiency of liquid adsorption inside the porous structure. The resulting water filling capacities based on the QCM are in good agreement with the measured porosity values for all three films. This indicates that polymer-swelling-assisted SIS allows a high degree of water adsorption inside the porous structures.

Note that the effective volume of pores filled with solvent gradually decreases with decreasing porosity. This is attributed to the loss of interconnectivity of the pores and the presence of closed pores not accessible for water and acetone. Therefore, we focus further on the analysis of the highly porous alumina film, with 70% porosity, and the approaches for controlling the water penetration inside it.

The effect of the amount of adsorbed water on oscillating frequency was further confirmed experimentally with partially blocked pores (figures 3(a) and (b)), in which we covered a fraction of the porous surface with single-layer graphene, which is recognized as a hydrophobic material [28]. Figures 3(c) and (d) represent schematically the water-filling capacity of the uncoated and graphene-coated porous alumina. The experiment on alumina partially coated with graphene was conducted to probe the connectivity and directionality of the pores.

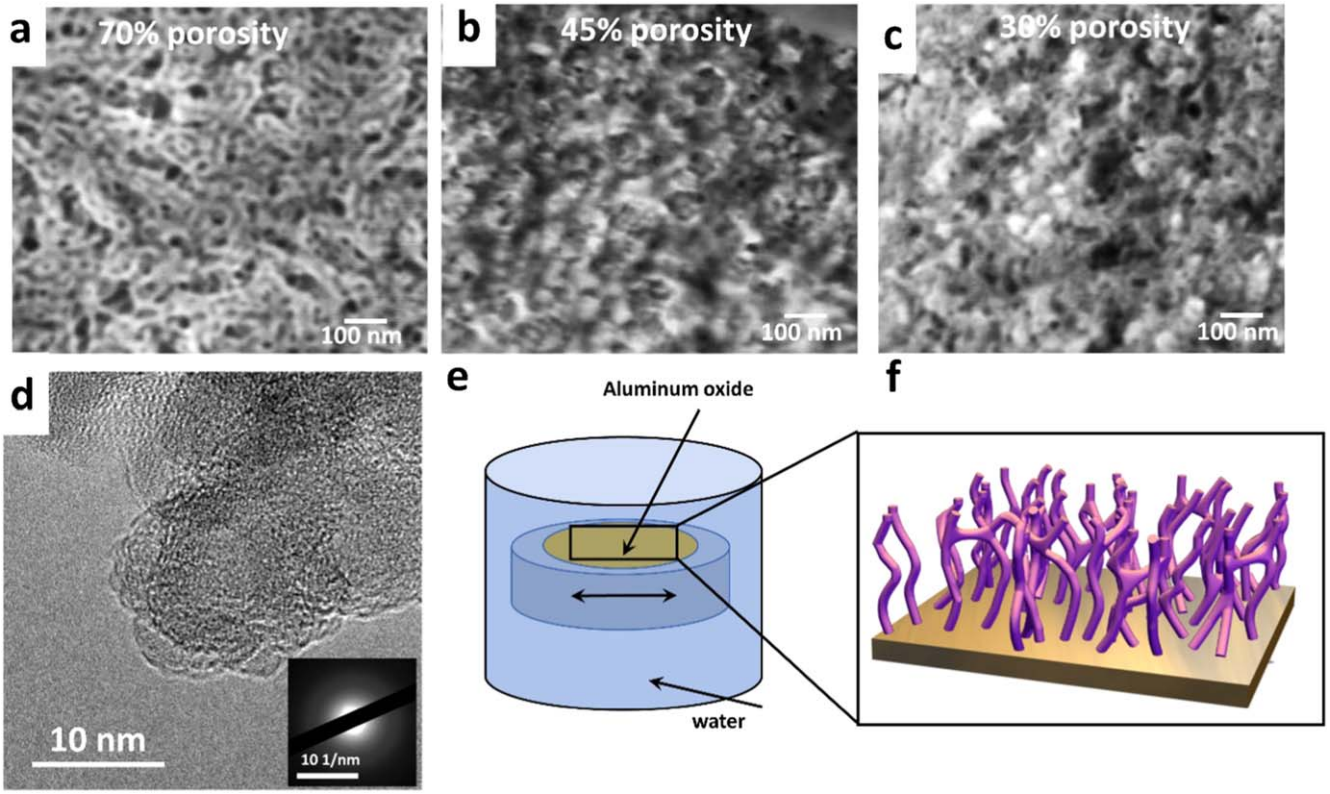

Figure 1. SEM images of the porous alumina films with (a) 70% porosity, (b) 45% porosity, and (c) 30% porosity. (d) HRTEM image and electron diffraction (inset) obtained from a fragment of porous alumina (70% porosity); (e) depiction of the QCM experiment; (f) schematic of the nanoporous alumina film on the substrate.

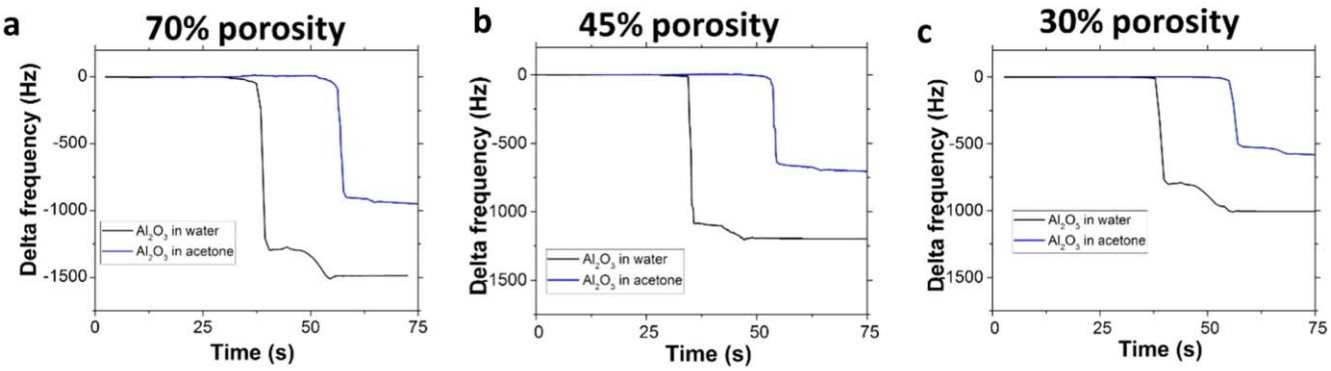

d

Sample	Viscosity effect (Hz)	Liquid in pores effect (Hz)	Effective volume of pores with solvent, %
70% Al_2O_3 in water	-715	-780	98%
70% Al_2O_3 in acetone	-360	-580	94%
45% Al_2O_3 in water	-715	-479	93%
45% Al_2O_3 in acetone	-360	-336	84%
30% Al_2O_3 in water	-715	-292	85%
30% Al_2O_3 in acetone	-360	-220	83%

Figure 2. Change in resonant frequency of the nanoporous alumina-coated QCM with (a) 70%, (b) 45%, and (c) 30% porosity. (d) Summary of the frequency shift values and estimates for the effective volume of pores filled with solvent.

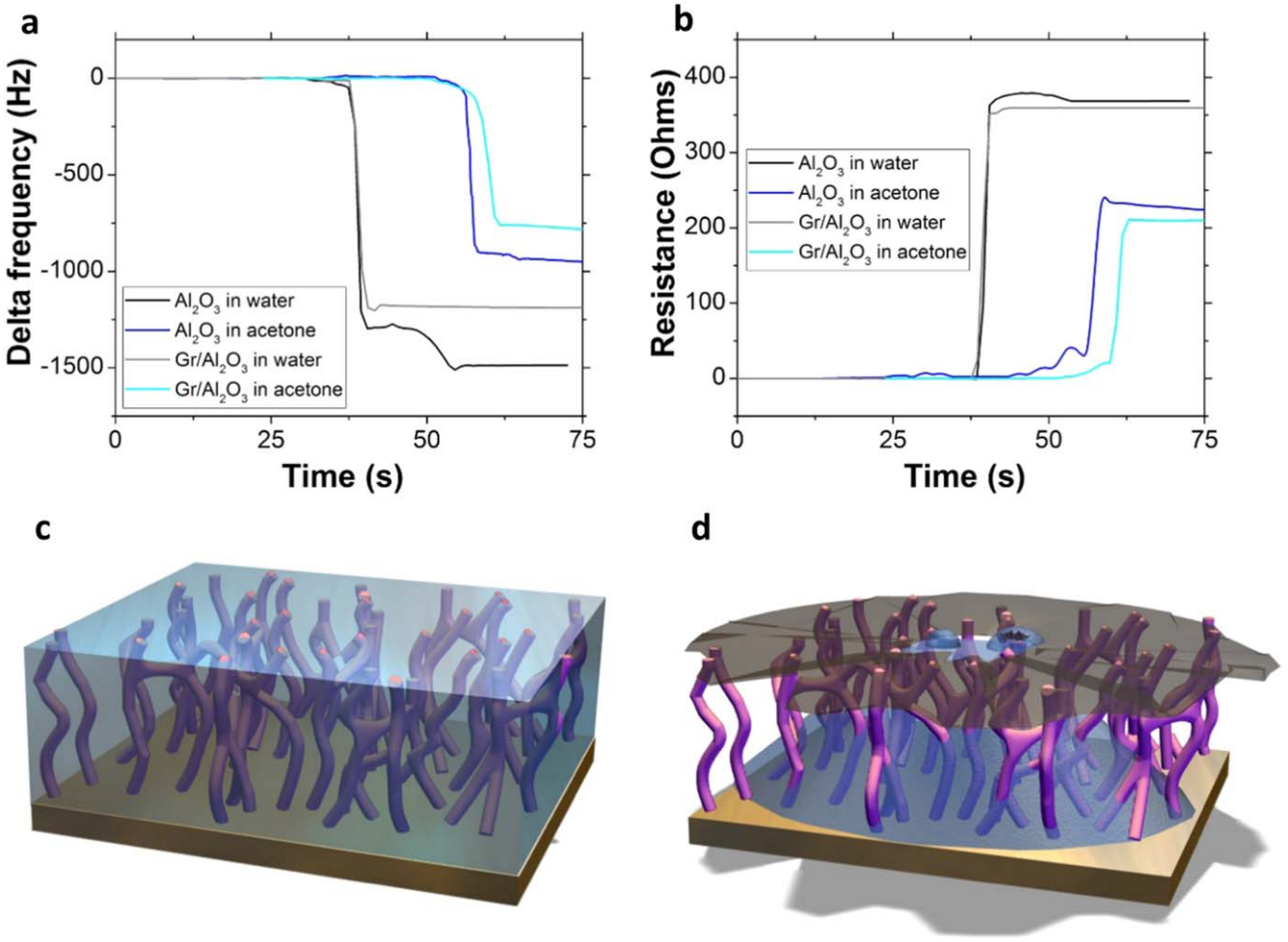

Figure 3. Change in (a) resonant frequency and (b) mechanical resistance of the nanoporous alumina (70% porosity) coated QCM upon immersion in water and acetone without and with graphene film on top. Schematics of the water penetration in (c) nanoporous alumina and in (d) graphene with defects on nanoporous alumina.

Suspended graphene was reported to be non-transparent for water molecules [29]. As a result, water can enter the structure only via unprotected area of alumina. Note that after deposition of the graphene, all samples were baked at 90 °C and tested within a day to eliminate the effect of graphene contamination that can affect wettability properties [30–32]. If penetration of the solvent into pores results in such a high shift in frequency, blocking the pores should also be detectable through the change in the QCM response. Indeed, as indicated in figure 1, graphene coating enabled lowering of the observed shifts both in resonant frequency and mechanical resistance towards the theoretically expected values. When a single-layer of graphene covered ∼80% of the geometrical surface of porous alumina, the effective volume of the pores field with solvents is estimated to be ∼60% (table 1). This indicates that even though the pores have directionality, they are highly interconnected. Table 1 summarizes the observed results and summarizes the filling capacity of the nanoporous alumina film without and with graphene. Note, that a similar trend is observed for both water and acetone.

Penetration of the solvent inside the pores also affects the mechanical resistance change of the QCM surface. Equation (2) assumes that a well-defined interface between the QCM and liquid acts as a liquid coupling line. In this case, the interfacial velocity of the liquid equals the velocity of the oscillating QCM surface and decays to zero when moving away from the surface. In case of the porous structure, the liquid/QCM interface is widened to the thickness of the porous film (∼200 nm), thereby leading to partial coupling/partial slippage of the water inside [33]. Only the porous surface velocity of the liquid decays as would be expected. The surface area of the porous alumina is estimated to be ∼200 m^2 per gram of material. The estimation is made based on the the water adsorption inside the 200 nm thick alumina films with available pores of a characteristic size of ∼20 nm (figure 1).

Interestingly, once the sample is removed from the water, the area covered by graphene dries out immediately, while the area without graphene, where bare nanoporous alumina was exposed to water, keeps water trapped inside (figure 4). Our results demonstrate that porous alumina is very hydrophilic, not only leading to the low water contact angle of 33.1°±1.7°, but also resulting in water residue upon removing the sample from the liquid (figure 4(a) highlights the presence of water droplets on the surface not covered with graphene. Note that

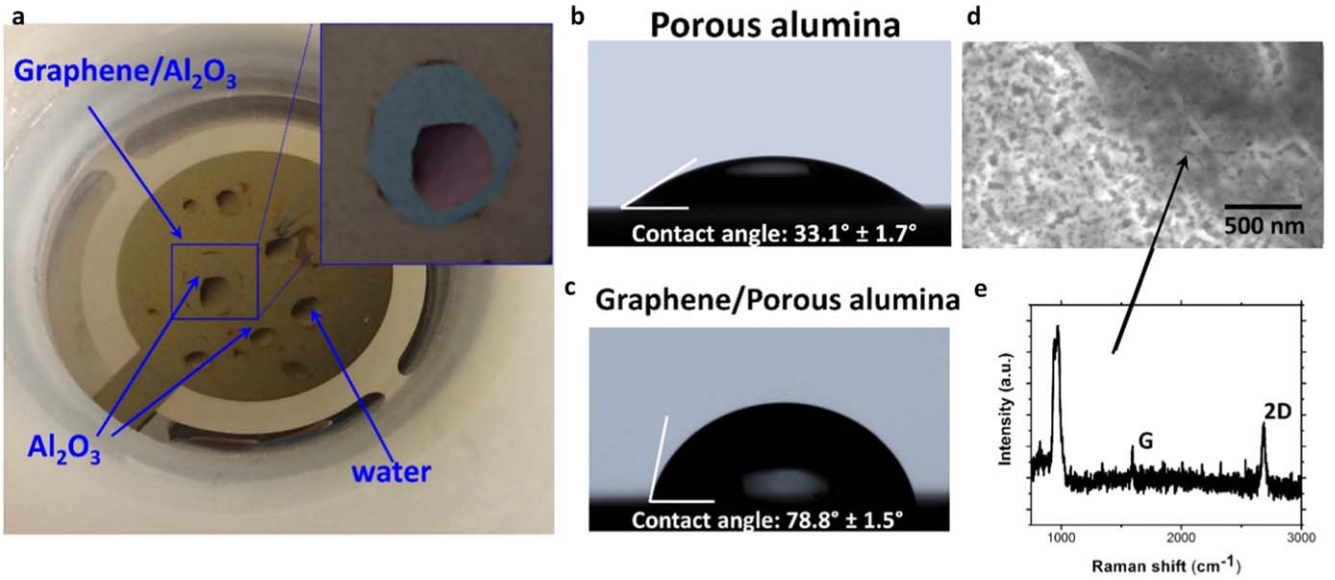

Figure 4. (a) Photo of the graphene-coated nanoporous alumina QCM surface immediately after its removal from water. Residual water droplets in the areas of graphene tearing (non-graphene covered alumina) are observed. The false color inset highlights the areas representing graphene (brown), bare alumina (gray) and residual water (purple). Water contact angle measurements for (b) porous alumina and (c) graphene on top of porous alumina are presented to demonstrate graphene coverage preventing water penetration. (d) SEM image of the graphene on a nanoporous alumina surface indicates high contrast of the edge area with (e) Raman spectrum confirming a single layer of graphene.

Table 1. Comparison of viscosity and added mass effects on the resonant frequency change of the porous alumina-coated QCM upon immersion in water and acetone without and with graphene. The effective volume of pores is calculated by normalization of the weight of the adsorbed water by the total volume estimated for 200 nm thick alumina with 70% porosity.

Sample (70% porosity)	Viscosity effect (Hz)	Liquid in pores effect (Hz)	Effective volume of pores filled with solvent, %
Al_2O_3 in water	−715	−780	98%
Al_2O_3 in acetone	−360	−580	94%
Gr/Al_2O_3 in water	−715	−480	60%
Gr/Al_2O_3 in acetone	−360	−400	64%

the water contact angle for the bulk alumina was reported to be in the range of 80° to 90° [34]. Our results demonstrate a significant increase in hydrophilicity of porous alumina as compared to its bulk analogs [34] as well as to solid crystalline alumina film deposited by 200 atomic layer deposition (ALD) cycles following the regular ALD procedure [35] (figure 5(a)). This observation can be attributed to increased hydrophilicity of the surface, allowing the porous alumina structure to act as a sponge, highly adsorbing the liquid and, in turn, lowering the water contact angle.

Surprisingly, the water contact angle on the deposited single-layer graphene is significantly higher than that of bare porous alumina (78.8°±1.5°). At first glance, in this case the high contact angle is somewhat expected given the known hydrophobicity [28] of graphene. However, previously, Rafiee *et al* reported water transparency of the graphene for surfaces interacting with water by van der Waals interactions [36]. The value of water contact angle on single-layer graphene was nearly the same as on the solid graphene support, and supported graphene reveals its own water contact angle only when its thickness exceeds 6 monolayers [36]. Our results indicate that porous support does not significantly impact the wettability of single-layer graphene, probably as a result of the small number of interfacial contacts between porous alumina and graphene. Also, our results support the previously reported data that the wettability of graphene is determined mainly by short-range graphene–liquid interactions since about 80% of the long-range water–substrate interactions are screened by the graphene monolayer [37].

In control experiments with uncoated and single-layer graphene-coated nonporous alumina-coated QCMs obtained by 200 ALD cycles, we obtained water contact angles of 84.6°±1.7° and 83.2°±1.5°, respectively (figure 5). These values are similar to those of solid alumina surfaces [34] and single-layer graphene deposited onto lithographically nanotextured surfaces [37], respectively. The resulting frequency and mechanical resistance changes are in accordance with theoretically predicted values and only a slight modification can be attributed to roughness and contamination effects. When graphene is deposited on top of nonporous alumina, the differences in both frequency and resistance are minimal and can be attributed to residual contamination of graphene on the edges of the sample, acting possibly as an additional water trapping region [38, 39].

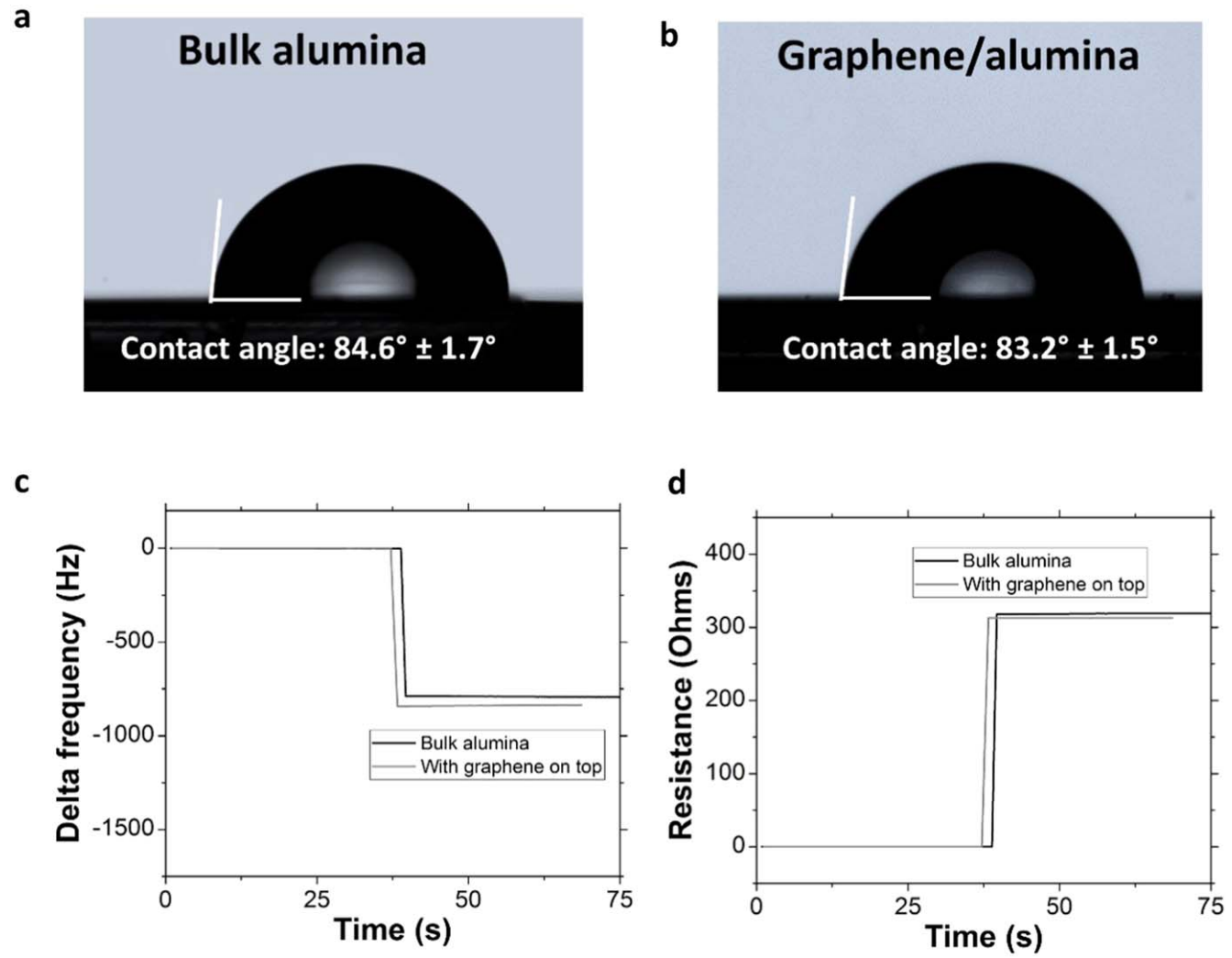

Figure 5. Water contact angle measurements for (a) solid alumina film grown by 200 ALD cycles and (b) graphene on solid alumina film grown by 200 ALD cycles. QCM monitoring of the (c) delta frequency change and (d) resistance change upon immersion in water. A slight change in frequency is attributed to the presence of tearing in graphene leading to a small amount of water encapsulation on the surface. Small variations in the figures for bulk alumina and for porous alumina are attributed to partial defects in the graphene film.

Alumina is widely recognized as a promising material for monitoring humidity [40–42]. Since alumina prepared via SIS is highly porous and its surface is hydrophilic enabling rapid infiltration of its pores by water, we tested its ability to sense humidity at atmospheric pressure and room temperature using the QCM technique. Figure 6 summarizes QCM resonant frequency change when the system is inserted into a vacuum chamber and humidity is introduced gradually in the form of water vapor. Adsorption of water vapors on the surface of the nanoporous structure of the QCM results in a significant change in resonant frequency response when exposed to low relative humidity values; in contrast, solid alumina films obtained by 200 ALD cycles do not respond to small humidity variation. Similar contrast difference for bulk and porous structures has already been explored by Lazarovich *et al* [42]. Previously, 13 μm thick nanoporous alumina films produced by anodizing the bulk QCM electrode material were used to sense the presence of the water vapors [42]. Here, we demonstrate the high sensitivity of 200 nm thick nanoporous alumina films, attributed to the interconnectivity of the pores in SIS-produced alumina films. After normalization by the thickness, the alumina prepared by polymer-swelling-assisted SIS reveals 7 times higher sensitivity toward the water than porous alumina prepared by anodization.

Previous studies indicated that the wetting characteristics of the surfaces are affected by the surface roughness profile and surface energy. When the surface energy of the material is higher than that of water, water wets the surface more easily [44, 45]. Oxygenation of the surfaces was reported to increase the surface energy of materials [46, 47]. The XPS analysis of the survey scans for bulk and porous alumina surfaces indicates a higher concentration of oxygen in case of the porous film (figures 6(b) and (d)). We attribute such a variation in the oxygen concentration to the amorphous nature of the porous alumina developed by SIS which allows the higher presence of oxygen groups in the defect sites. The increased roughness profile of nanoporous alumina is an additional contributor to the material's hydrophilicity with the contact angle of the

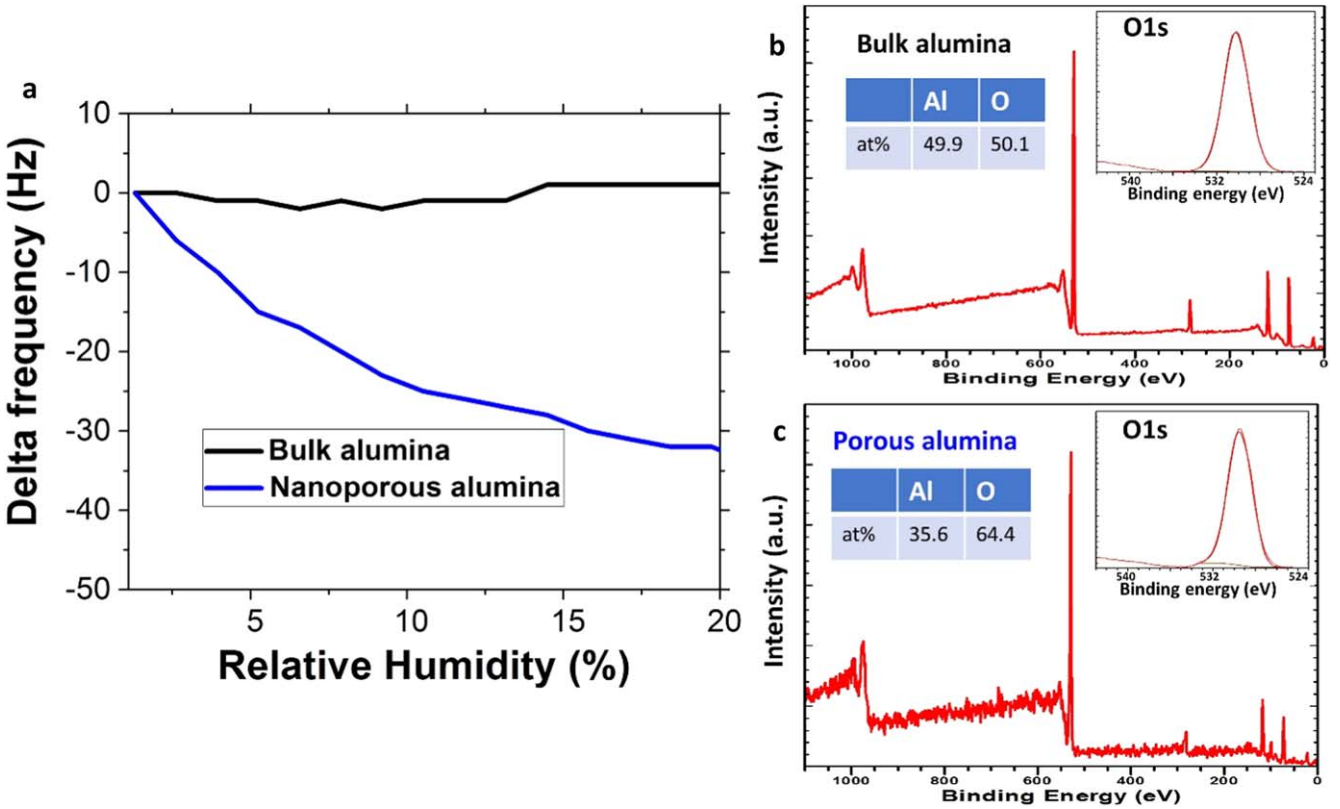

Figure 6. QCM monitored water vapor adsorption. (a) In contrast to bulk alumina electrode, SIS designed nanoporous alumina detects the presence of humidity at earlier stages, as is indicated by the gradual decrease in resonant frequency. In the case of bulk alumina, only a slight change of resonant frequency around the initial value is observed. XPS analysis of the (b) bulk and (c) porous alumina indicates the higher presence of oxygen groups in porous alumina. The presence of a small carbon peak in the XPS spectra of bulk and porous alumina films is attributed to adventitious carbon usually observed for samples exposed to air [43].

smooth surface being less than 90° [48]. The combined effect of the surface roughness increase and surface energy increase of the nanoporous alumina surface thus results in excellent wetting characteristics of SIS-developed materials and causes the high efficiency of water adsorption and penetration in the pores.

4. Conclusions

Here we report on high wetting and solvent adsorption characteristics of porous alumina developed by the polymer-swelling-assisted infiltration technique. Using an ultra-sensitive QCM approach we explored the accessibility of the pores for water and acetone penetration. The estimated surface area of the resulting nanoporous alumina structures is 200 m^2 per gram of material. We also show that pores are highly interconnected, and even blocking of ~80% of the porous surface by a single-layer graphene film still allows solvent penetration in ~60% of all available pore volume. Since the SIS approach is compatible with a broad range of surfaces, the highly porous coating can be deposited onto the surface of a QCM to allow for probing the kinetics of solvent infiltration with high sensitivity. Using humidity detection as an example, we demonstrated that polymer-swelling-assisted SIS is a promising approach for designing materials for sensing applications.

Acknowledgments

This work was performed in part at the University of North Texas' Materials Research Facility. Support from the Advanced Materials and Manufacturing Processes Institute (AMMPI) at the University of North Texas is acknowledged. Work at the Center for Nanoscale Materials was supported by the U S Department of Energy, Office of Science, Office of Basic Energy Sciences, under Contract No. DE-AC0206CH-11357.

ORCID iDs

Diana Berman https://orcid.org/0000-0002-9320-9772

References

[1] Xi J Q, Schubert M F, Kim J K, Schubert E F, Chen M, Lin S-Y, Liu W and Smart J A 2007 Optical thin-film

materials with low refractive index for broadband elimination of Fresnel reflection *Nat. Photon.* **1** 176–9
[2] Zhao M, Yang Z Y, Zhu D Q, Jin X and Huang D X 2005 Influence of the fabrication technique on the porous size of the polymer nanoporous antireflection coatings *J. Opt. Soc. Am.* B **22** 1330–4
[3] Shin H-C and Liu M 2004 Copper foam structures with highly porous nanostructured walls *Chem. Mater.* **16** 5460–4
[4] Perez-Ramirez J, Christensen C H, Egeblad K, Christensen C H and Groen J C 2008 Hierarchical zeolites: enhanced utilisation of microporous crystals in catalysis by advances in materials design *Chem. Soc. Rev.* **37** 2530–42
[5] Perego C and Millini R 2013 Porous materials in catalysis: challenges for mesoporous materials *Chem. Soc. Rev.* **42** 3956–76
[6] Jin Z, Zhou H-J, Jin Z-L, Savinell R F and Liu C-C 1998 Application of nano-crystalline porous tin oxide thin film for CO sensing *Sensors Actuators* B **52** 188–94
[7] Mariani S, Pino L, Strambini L M, Tedeschi L and Barillaro G 2016 10 000-fold improvement in protein detection using nanostructured porous silicon interferometric aptasensors *ACS Sensors* **1** 1471–9
[8] Chudasama C D, Sebastian J and Jasra R V 2005 Pore-size engineering of zeolite a for the size/shape selective molecular separation *Ind. Eng. Chem. Res.* **44** 1780–6
[9] Furukawa H, Gándara F, Zhang Y-B, Jiang J, Queen W L, Hudson M R and Yaghi O M 2014 Water adsorption in porous metal–organic frameworks and related materials *J. Am. Chem. Soc.* **136** 4369–81
[10] Li F, Zhang L and Metzger R M 1998 On the growth of highly ordered pores in anodized aluminum oxide *Chem. Mater.* **10** 2470–80
[11] Gulati K, Santos A, Findlay D and Losic D 2015 Optimizing anodization conditions for the growth of titania nanotubes on curved surfaces *J. Phys. Chem.* C **119** 16033–45
[12] Trimm D L and Stanislaus A 1986 The control of pore size in alumina catalyst supports: a review *Appl. Catalysis* **21** 215–38
[13] Li S, Wang C-A and Zhou J 2013 Effect of starch addition on microstructure and properties of highly porous alumina ceramics *Ceram. Int.* **39** 8833–9
[14] Shi J, Wang Y, Yang W, Tang Y and Xie Z 2015 Recent advances of pore system construction in zeolite-catalyzed chemical industry processes *Chem. Soc. Rev.* **44** 8877–903
[15] Roth W J *et al* 2013 A family of zeolites with controlled pore size prepared using a top-down method, Nature *Chemistry* **5** 628–33
[16] Tsuchiya H and Schmuki P 2005 Self-organized high aspect ratio porous hafnium oxide prepared by electrochemical anodization *Electrochem. Commun.* **7** 49–52
[17] Shin H-C, Dong J and Liu M 2004 Porous tin oxides prepared using an anodic oxidation process *Adv. Mater.* **16** 237–40
[18] Tsui L-K and Zangari G 2014 Titania nanotubes by electrochemical anodization for solar energy conversion *J. Electrochem. Soc.* **161** D3066–77
[19] Peng Q, Tseng Y C, Darling S B and Elam J W 2010 Nanoscopic patterned materials with tunable dimensions via atomic layer deposition on block copolymers *Adv. Mater.* **22** 5129–33
[20] Peng Q, Tseng Y-C, Darling S B and Elam J W 2011 A route to nanoscopic materials via sequential infiltration synthesis on block copolymer templates *ACS Nano* **5** 4600–6
[21] Tseng Y-C, Peng Q, Ocola L E, Elam J W and Darling S B 2011 Enhanced block copolymer lithography using sequential infiltration synthesis *J. Phys. Chem.* C **115** 17725–9
[22] Berman D, Guha S, Lee B, Elam J W, Darling S B and Shevchenko E V 2017 Sequential infiltration synthesis for the design of low refractive index surface coatings with controllable thickness *ACS Nano* **11** 2521–30
[23] She Y, Lee J, Diroll B T, Lee B, Aouadi S, Shevchenko E V and Berman D 2017 Rapid synthesis of nanoporous conformal coatings via plasma-enhanced sequential infiltration of a polymer template *ACS Omega* **2** 7812–9
[24] Lee J, Hu X, Voevodin A A, Martini A and Berman D 2018 Effect of substrate support on dynamic graphene/metal electrical contacts *Micromachines* **9** 169
[25] Kanazawa K K and Gordon J G 1985 Frequency of a quartz microbalance in contact with liquid *Anal. Chem.* **57** 1770–1
[26] Arnau A, Sogorb T and Jiménez Y 2002 Circuit for continuous motional series resonant frequency and motional resistance monitoring of quartz crystal resonators by parallel capacitance compensation *Rev. Sci. Instrum.* **73** 2724–37
[27] Martin S J, Granstaff V E and Frye G C 1991 Characterization of a quartz crystal microbalance with simultaneous mass and liquid loading *Anal. Chem.* **63** 2272–81
[28] Taherian F, Marcon V, van der Vegt N F A and Leroy F 2013 What is the contact angle of water on Graphene? *Langmuir* **29** 1457–65
[29] Berry V 2013 Impermeability of graphene and its applications *Carbon* **62** 1–10
[30] Li Z *et al* 2013 Effect of airborne contaminants on the wettability of supported graphene and graphite *Nat. Mater.* **12** 925
[31] Kozbial A, Trouba C, Liu H and Li L 2017 Characterization of the intrinsic water wettability of graphite using contact angle measurements: effect of defects on static and dynamic contact angles *Langmuir* **33** 959–67
[32] Kozbial A, Li Z, Sun J, Gong X, Zhou F, Wang Y, Xu H, Liu H and Li L 2014 Understanding the intrinsic water wettability of graphite *Carbon* **74** 218–25
[33] Coffey T and Krim J 2005 Quartz-crystal microbalance studies of the slippage of solid and liquid krypton monolayers on metal(111) and ${/mathrm{C}}_{60}$ surfaces *Phys. Rev.* B **72** 235414
[34] Buijnsters J G, Zhong R, Tsyntsaru N and Celis J-P 2013 Surface wettability of macroporous anodized aluminum oxide *ACS Appl. Mater. Interfaces* **5** 3224–33
[35] Ylivaara O M E *et al* 2014 Aluminum oxide from trimethylaluminum and water by atomic layer deposition: the temperature dependence of residual stress, elastic modulus, hardness and adhesion *Thin Solid Films* **552** 124–35
[36] Rafiee J, Mi X, Gullapalli H, Thomas A V, Yavari F, Shi Y, Ajayan P M and Koratkar N A 2012 Wetting transparency of graphene *Nat. Mater.* **11** 217–22
[37] Ondarçuhu T, Thomas V, Nuñez M, Dujardin E, Rahman A, Black C T and Checco A 2016 Wettability of partially suspended graphene *Sci. Rep.* **6** 24237
[38] Lee J, Atmeh M and Berman D 2017 Effect of trapped water on the frictional behavior of graphene oxide layers sliding in water environment *Carbon* **120** 11–6
[39] Lee J and Berman D 2018 Inhibitor or promoter: insights on the corrosion evolution in a graphene protected surface *Carbon* **126** 225–31
[40] Chen Z and Lu C 2005 Humidity sensors: a review of materials and mechanisms *Sensor Letters* **3** 274–95
[41] Farahani H, Wagiran R and Hamidon M 2014 Humidity sensors principle, mechanism, and fabrication technologies: a comprehensive review *Sensors* **14** 7881
[42] Lazarowich R J, Taborek P, Yoo B-Y and Myung N V 2007 Fabrication of porous alumina on quartz crystal microbalances *J. Appl. Phys.* **101** 104909
[43] Miller D, Biesinger M and McIntyre N 2002 Interactions of CO2 and CO at fractional atmosphere pressures with iron

and iron oxide surfaces: one possible mechanism for surface contamination? *Surf. Interface Anal.* **33** 299–305

[44] Wenzel R N 1936 Resistance of solid surfaces to wetting by water *Ind. Eng. Chem.* **28** 988–94

[45] Yoshimitsu Z, Nakajima A, Watanabe T and Hashimoto K 2002 Effects of surface structure on the hydrophobicity and sliding behavior of water droplets *Langmuir* **18** 5818–22

[46] Cioffi M O H, Voorwald H J C and Mota R P 2003 Surface energy increase of oxygen-plasma-treated PET *Mater. Charact.* **50** 209–15

[47] Mattox D M 2010 *Handbook of Physical Vapor Deposition (PVD) Processing* (Norwich, NY: William Andrew)

[48] Wang X and Yoshimura N 1999 Fractal phenomena. Dependence of hydrophobicity on surface appearance and structural features of SIR insulators *IEEE Trans. Dielectr. Electr. Insul.* **6** 781–91